2D Materials

OPEN ACCESS

RECEIVED
29 November 2016

REVISED
6 March 2017

ACCEPTED FOR PUBLICATION
15 March 2017

PUBLISHED
19 April 2017

PAPER

A thermally-invariant, additively manufactured, high-power graphene resistor for flexible electronics

Monica Michel[1], Chandan Biswas[2], Chandra S Tiwary[3], Gustavo A Saenz[2], Ridwan F Hossain[2], Pulickel Ajayan[3] and Anupama B Kaul[2]

[1] Metallurgical, Materials and Biomedical Engineering Department, University of Texas at El Paso, El Paso, TX 79968, United States of America
[2] Electrical and Computer Engineering Department, University of Texas at El Paso, El Paso, TX 79968, United States of America
[3] Materials Science and Nano Engineering Department, Rice University, Houston, TX 77005, United States of America

E-mail: akaul@utep.edu

Keywords: TCR, 2D graphene ink, ink jet printing, high power resistor

Abstract

Solution processed two-dimensional (2D) layered materials and their integration with additive manufacturing techniques, such as ink-jet printing, is a facile approach for incorporating these exotic materials into device platforms for flexible electronics. In this work, graphene ink formulations are successfully utilized toward the design and fabrication of high-power resistive structures that are printed on both rigid and flexible substrates and have the potential to deliver close to 10 W of power. A near-flat, negative temperature coefficient of resistivity (TCR) is measured with an activation energy $E_a \sim 2.4$ meV for electron hopping, which is 100× lower compared to E_a values for high TCR materials. The TCR and E_a values are amongst the lowest reported for 2D layered material systems. The thermal-invariance of resistivity for such high-power graphene printed resistors is attractive for applications, for example to provide a stable heating source for flexible electronics over extreme thermal environments. The transport characteristics of the ink-jet printed features is modeled as a composite structure in order to explain the thermal response which appears to be mediated via defects in the sonicated graphite, and correlates well to inferences made from Raman spectroscopy and transmission electron microscopy analysis conducted on the printed graphene structures. In order to fabricate such functional structures with ink-jet printing, the active nozzle number, printing passes, and annealing conditions are shown to play an important role to determine line resolution, and also dictate the morphological and electronic transport characteristics of the printed graphene features.

Continuous miniaturization of devices, for example in consumer electronics, defense and aerospace applications, is largely driven by our desire for smaller, light-weight, ultra-thin devices, where such structures on fully flexible platforms can drive down costs even further [1, 2]. For flexible electronics applications in particular, the substrates pose less restrictions compared to the Si-based semiconductor industry, where in the former, a wide variety of additive manufacturing techniques easily lend themselves for the production of functional structures on arbitrary substrates within the context of what is generally referred to as 'printed electronics.' Examples of functional printed structures include printed batteries, solar cells, light emitting diodes that have been formed using organic and inorganic materials [3, 4]. One commonly used additive manufacturing technique for printed electronics is ink-jet printing, which allows for a fast and cheap approach for patterning electronic devices, circuits and systems using a range of inks [5], from metallic to semiconducting, to construct active or passive structures [6].

With the advent of two-dimensional (2D) layered materials (LMs), which includes quintessential 2D graphene, solution dispersions of 2DLMs have been formulated recently for ink-jet printing [7–10]. Although great progress has been made to produce liquid dispersions of 2DLMs, challenges still lie in the reliable mass production of these materials for practical applications. Some of the techniques used for solution-based exfoliation include intercalant assisted exfoliation [11, 12], thermal shock [13], or shear oxidation of graphite [14] although the oxidation process results in structural defects and dispersions that are often

electrically insulating [15]. It is important to note that a significant fraction of the studies are actually conducted on graphene oxide and not necessarily graphene to form the graphene ink [16, 17]. Other challenges are related to the low-density of the dispersions which do not yield electrically conductive films [18], or the presence of residues that traditional solvents and surfactants leave, which compromises the electrical conductivity [19]. In addition, there is little work done on systematically studying the effect of printing parameters on the quality of the printed 2DLM features, as well as their structural, morphological and electrical transport properties.

In this work, we have conducted a systematic investigation of the ink-jet printing parameters that sheds insights into the characteristics of the printed features, and we have successfully utilized these inks for fabricating practical devices that display unique characteristics, specifically, the ability to deliver ultra-high levels of power using ink-jet printed graphene resistors. We have also determined that the active nozzle number, printing passes, and annealing conditions have an important role to play in determining printed line resolution, as well as the morphological and electronic transport characteristics of the printed graphene features, where the inks are generated via sonication of the bulk graphite crystal. Here the inks are dispersed drop-by-drop in pico-liter volumes using drop-on-demand ink-jet printing technology, to construct macro-scale device architectures onto a wide range of substrates, from rigid to flexible and transparent. As mentioned, the formulations were used toward the successful fabrication of a high-power multilayer graphene resistive structure that was printed on both rigid and flexible substrates, and can deliver power levels approaching 10 W, where a near-flat, negative temperature coefficient of resistivity (TCR) was measured.

The change in resistance R with respect to an increase in temperature T of a material, as denoted by the TCR, is positive for $R \propto T$ or negative where $R \propto 1/T$. The activation energy E_a was computed to be ~2.4 meV for our ink-jet printed multilayer graphene resistors, which is 100× lower compared to high TCR materials [20] such as mechanically exfoliated graphene, for measurements we conducted in the 6 K–350 K range. Interestingly, previous studies have shown the possibility of using the temperature-dependent electrical properties of graphene as a temperature sensor [21]. In other studies, positive and negative TCR materials have been combined to achieve a near-zero-(NZ-) TCR bilayer composite structure [22]. Resistors having NZ-TCR are desirable for various applications, such as analog and data conversion circuits, specialty instrumentation circuits, and static random access memories (SRAMs) [23]. High-power resistors that can dissipate many Watts of electrical power as heat may be used as part of motor controls, in power distribution systems, or as test loads for generators. While one-dimensional (1D) carbon nanotube based systems demonstrate a NZ-TCR, our results show the TCR and E_a to be the lowest amongst the 2DLMs reported to date. We have modeled the transport characteristics of our ink-jet printed features as a composite structure made up of remnant ethyl cellulose (EC) used in the solution dispersion as a surfactant, not to mention the graphene nanomembranes that contribute toward the composite behavior as well. The unique microstructure of our printed nanocomposite was used as a basis upon which to explain the thermal response of the electronic transport of our devices that we believe is mediated via defects in the sonicated graphite. Evidence for defects was validated via Raman spectroscopy and transmission electron microscopy of our ink-jet printed graphene nanomembranes. The thermal-invariance of resistivity or a small TCR exhibited by our devices has utility as a component in flexible electronics where a stable current or heat-load load maybe necessary in harsh or extreme thermal environments.

Results and discussion

A stable dispersion of 2D graphene was formed through optimization detailed in earlier work, where we engineered the dispersion viscosity with the addition of surfactant EC in N-methyl-2-pyrrolidone (NMP) to prepare optimal dispersions [24, 25]. In figure 1, the effect of nozzle number on the printing resolution is provided, where an array of lines with 15 passes was printed on SiO_2/Si substrates using 16 (maximum for cartridge), 8, 4 and 2 nozzles, and annealing was conducted for 1 h at 300 °C. As it can be seen in figures 1(a)–(d), the line edge resolution and uniformity of the printed arrays improved as the number of active nozzles decreased from all 16 firing (figure 1(a)) to only 2 active nozzles printing (figure 1(d)). Printing with all 16 nozzles resulted in non-uniform line edges due to excessive volume of ink delivered that likely leads to ink spreading on the substrate, compromising line resolution. However, each printing system is unique, from the ink or printing fluid, the substrate, their respective temperatures, pretreatments, the firing voltage, waveform, and the rest of the specific printing conditions used. In our case, we kept all of the printing parameters constant, while the number of active nozzles firing was optimized in order to yield good line resolution. As mentioned, for our specific printing system, optimum printing resulted when 2 nozzles were used without modifying any of the other parameters. However, this determination of 2 nozzles being ideal is unique to our particular material system, and determination of the optimal nozzle number for other material systems, such as the specific inks or substrates used, may not necessarily be the same and needs to be validated experimentally.

We then proceeded to conduct 2-terminal current–voltage (I–V) measurements on the printed graphene films which were formed using 2 and 4 nozzles. Both of the samples exhibited linear Ohmic characteristics, as shown in figure 1(e), where

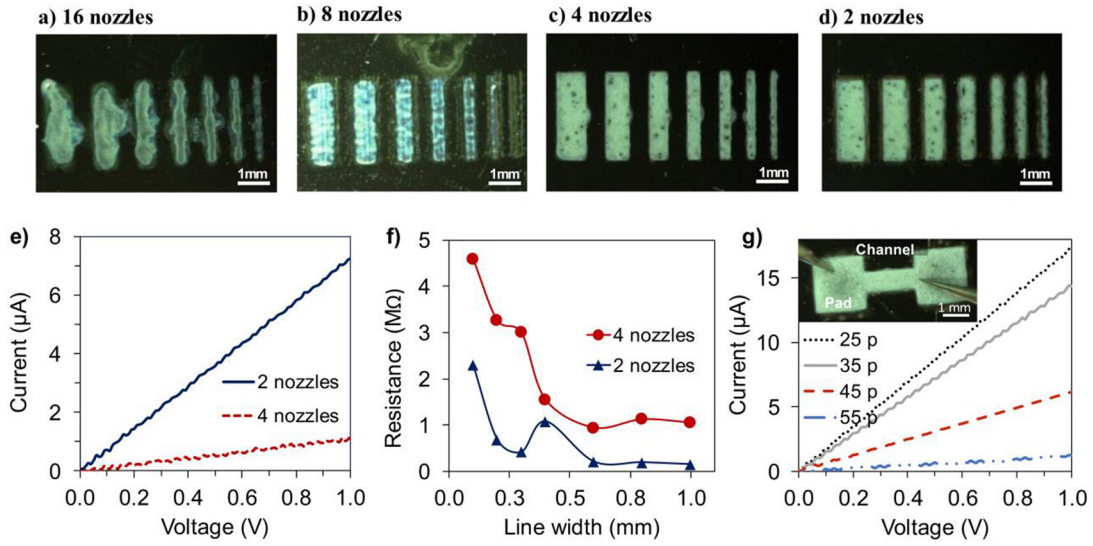

Figure 1. Printed line arrays with (a) 16, (b) 8, (c) 4, and (d) 2 nozzles. The printed array consisted of seven parallel lines that were 3 mm in length and spaced 0.8 mm apart, and the line width decreased from 1 mm to 0.1 mm. (e) *I–V* measurement of printed lines using 4 and 2 nozzles.(f) Change in resistance values with different printed line widths. The probe-tip separation in (e) and (f) was 1.5 mm. (g) *I–V* Characteristics comparing the effect of printing passes on the electronic transport. Inset showing printed pattern indicating channel (1.5 mm length, 0.5 mm width) and square pad (1.5 mm) sections.

the resistance in the 2 nozzle case was calculated to be 600 kΩ, which was 4× lower than the 4 nozzle case; printing with 8 or more nozzles yielded poor electronic transport characteristics, which is consistent with the poor film homogeneity and uniformity we observed (figures 1(a)–(d)) of the printed lines with increasing nozzle number. While keeping the number of printing passes fixed, the *R* was seen to decrease rapidly as the printed line width increased, as shown in figure 1(f) Graphene films printed with 2 nozzles exhibited consistently lower *R* values compared to 4 nozzles for all of the line widths explored here. Above linewidths of 0.5 mm, the *R* change remained unchanged with increasing line width, as shown in figure 1(f). The low *R* values noted in the 2 active nozzle case compared to the 4 nozzle case may have to do with the reduced ink volume deposited on the substrate which allows the solvent to evaporate more readily during the annealing step.

The effect of the number of printing passes was also examined here, where we conducted tests at 15, 25, 35, 45, 55 and 65, passes for ink printed on the SiO_2/Si substrate, and annealed at 300 °C for 1 h, as noted earlier, and measured the ensuing *I–V* Characteristic that is shown in figure 1(g); the inset in figure 1(g) shows the device geometry. It shows Ohmic behavior with maximal current transport occurring when 25 passes were used, where increasing passes of 35, 45 and 55 passes progressively decreased the currents, and no continuous channel was observed for 15 passes. In the case of 65 passes, no measurable current was obtained, due to remnant EC/solvent still present in the material. The above results on the printing parameters, such as number of active nozzles and printing passes clearly demonstrates the importance of optimizing these parameters to yield functional structures of 2DLMs using ink-jet printing.

We then proceeded to examine the role of the annealing temperature-time profile on the morphological and electronic transport characteristics for structures printed on SiO_2/Si substrates where 30 printing passes were used. The annealing temperatures considered were 250 °C, 300 °C, 350 °C, 400 °C and 450 °C, and two annealing times were used, 1 h and 2 h. The top-surface SEM images were obtained from the channel area and are shown in figures 2(a)–(c) and (e)–(g), while figures 2(d) shows the *R* variation as a function of the annealing temperature for the two times considered. The microstructure for the sample annealed for 1 h at 250 °C (figure 2(a)) shows random particles embedded in a matrix structure which is presumed to be remnant EC. Ethyl cellulose is a polymer that possesses excellent membrane-forming ability and durability and is commonly used as a flexible coating for paper, cloth and leather. However, at the same time, the electrical properties of EC indicate that it is electrically insulating, which corroborates the fact that the *R* for this sample was the highest at 2 MΩ, as noted in figure 2(d). Thus, the SEM in figure 2(a) shows the excessive presence of EC when a low annealing temperature of 250 °C was used. The microstructure of the samples that were annealed at higher temperatures (see figures 2(b)–(c)) shows that this potentially insulating matrix is largely removed (less charging is seen in the SEM images of figures 2(b) and (c) when compared to (a) for example), and a more uniform and conducting film has formed, which is corroborated by the lower *R* values seen in figure 2(d)

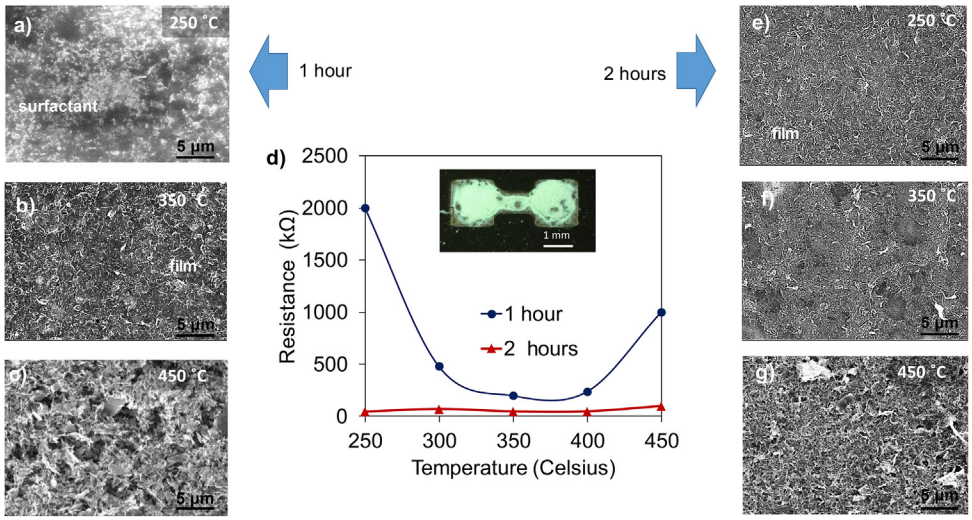

Figure 2. SEM images showing microstructure of the ink-jet printed lines after annealing for 1 h (a)–(c) and 2 h (e)–(g) at 250 °C, 350 °C and 450 °C, respectively, while (d) depicts the resistance variation with annealing temperature for the two different annealing times used.

for samples annealed at temperatures >300 °C. Figure 2(c) shows increased porosity in the microstructure for annealing temperature of 450 °C, which is consistent with the increased *R* values seen at 450 °C in figure 2(d). Annealing for 2 h at the same temperatures (250 °C–450 °C) resulted in a significant reduction in *R* values, as shown in figure 2(d). The *R* was reduced from 2 MΩ to 43 kΩ for samples annealed for 1 h and 2 h, respectively, at an annealing temperature of 250 °C. The corresponding microstructures depicted in figures 2(e)–(g) show more film uniformity at all temperatures, which correlates to the enhanced electrical conductance values (figure 2(d)), in contrast to the case where the samples were annealed for 1 h only. The longer annealing time likely accounts for the additional diffusion and coalescence of the nanomembranes to yield uniform films. The temperature-time profile of annealing on our samples demonstrated that while lower annealing temperatures can be traded for high-annealing temperatures, the annealing time has to increase to drive-off the excessive remnant solvent. This decrease in annealing temperature is advantageous to widen the portfolio of materials that would otherwise be precluded in flexible electronics, given thermal stability issues at higher temperatures in some of these materials systems.

To further build upon understanding the morphological characteristics of the ink-jet printed graphene films, figures 3(a)–(c) show high-resolution SEM images of the printed films that were annealed for 1 h at 250 °C, 350 °C and 450 °C, while figures 3(d)–(f) show the TEM images at these corresponding annealing conditions. The high resolution SEM images were obtained for ink-jet printed samples that were sectioned orthogonal to the plane of the substrate within the channel area (these sample images are shown in the top left insets of figures 3(a)–(c)), where cross sectional SEM images of the printed films were also obtained and are shown in the top-right insets of figures 3(a)–(c). The cross sectional image of the 250 °C heated sample shows a thick continuous film with graphene embedded in a matrix material which is likely to be remnant EC, as eluded to earlier. As the annealing temperature was increased to 350 °C (see figure 3(b), the graphene nanomembranes are denser and the surface morphology (middle right inset of figure 3(b)) reveals a uniform surface topography. When the annealing temperature was raised to 450 °C, the porosity of the films increased as voids were apparent (figure 3(c) inset on right), and the surface is notably rougher and less uniform (figure 3(c) inset on left middle). These results seem to be consistent with the electrical transport measurements of figure 2(d), which indicated 350 °C to be the optimum annealing temperature.

In order to conduct the TEM study of the ink-jet printed graphene films, Cu grids were used, and the TEM results are shown in figures 3(d)–(f). The TEM results once again revealed that the sample annealed at 250 °C showed graphene sheets embedded in a matrix material (EC/solvent), as shown in figure 3(d). As the annealing temperature was increased to 350 °C (figure 3(e)), the graphene membranes are clearly visible from the bright-field images, and a good intermembrane connection is noted, suggesting that the EC/solvent between them has been largely removed. The selected area diffraction (SAD) pattern of the sheets confirms the 0 0 2 orientation of multiple graphene sheets (shown in the top right inset in figure 3(e)). Finally, when the annealing temperature was increased to 450 °C, the presence of voids was noted to increase, as shown by the location of the arrows in the figure. The high magnification TEM images of figures 3(g) and (f), correspond to the annealing temperature of 350 °C, clearly reveal stacking of graphene layers with the interface marked with arrows. The presence of the dark islands within the graphene membranes in figures 3(e) and (f), is suggestive of defective

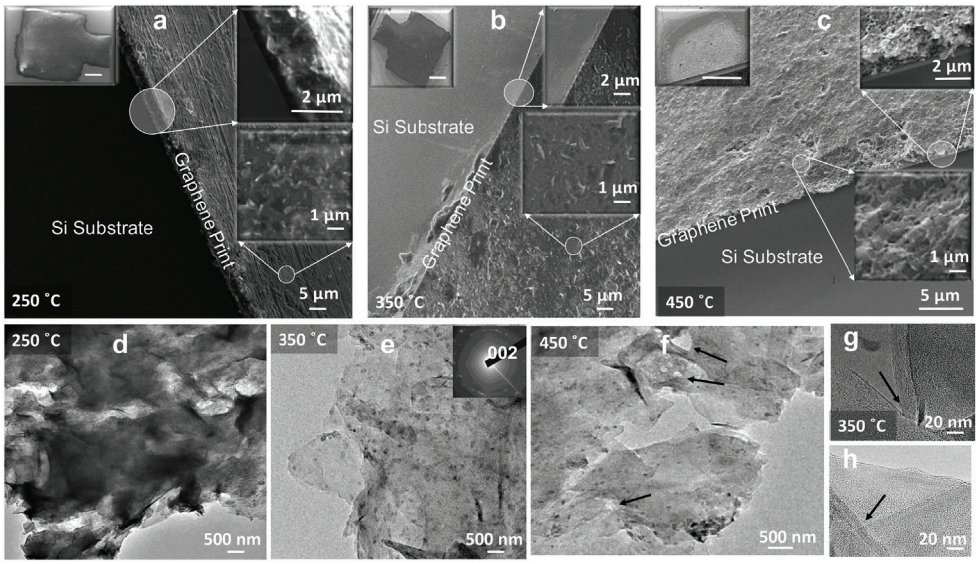

Figure 3. SEM images showing the interface between printed sample and SiO_2/Si substrate for 1 h annealed samples at (a) 250 °C, (b) 350 °C and (c) 450 °C. Left top insets in (a)–(c) show low magnification images of the sectioned sample (scale bar ~0.5 mm). The high magnification cross sectional SEM images (top right in (a)–(c)) reveal the interfacial characteristics between the ink-jet printed graphene and the SiO_2/Si substrate. The right bottom inset images show the surface morphology in (a)–(c). In (d)–(f), bright field TEM images of the printed graphene film are shown for samples annealed at 250 °C, 350 °C, and 450 °C, respectively. Arrows in (f) depict the presence of voids. The stacking of the graphene sheets is seen in (g)–(h) for the 350 °C annealing time where arrows show the stacked graphene nanomembrane junctions.

sites, which may be due to remnant residues from the solution dispersions, and we discuss this in more detail in the context of the temperature dependent response of the resistivity of our printed films.

Our ink-jet printed graphene films were further characterized using Raman spectroscopy, as well as temperature-dependent Raman, which is a non-invasive technique used to characterize the structural and electronic properties of materials [26]. The Raman shift is depicted in figure 4(a) for samples annealed at temperatures ranging from 200 to 450 °C, which shows the well-defined D band (1350 cm^{-1}), G band (1580 cm^{-1}) and a 2D or G′ band (2700 cm^{-1}), indicating the presence of monolayer or few-layer graphene. The D band has been attributed to in-plane A_{1g} zone-edge mode [27] and can be used to monitor the defect distribution of multilayer graphene films by computing the D/G ratio [28]. Conductivity data has not been reported for the sample annealed at 200 °C due to its excessively high R that was beyond the scope of the instrumentation. The defect ratios for samples annealed at 1 h and 2 h in figure 4(b) demonstrate the films with the lowest D/G values occur for samples annealed at 350 °C for 1 h, and 300 °C for 2 h which is consistent with our electrical data (figure 2(d))), where the lowest R values were seen at these conditions. Furthermore, the full-width-half-maximum (FWHM) of the D band is used to monitor defect distribution in graphene films [29]. The D band showed a maximum FWHM of ~99 cm^{-1} for samples annealed at 250 °C, which decreased to ~40 cm^{-1} for annealing at 350 °C, as seen in figure 4(b). This further verifies that the minimum defect distribution in the ink-jet printed graphene films occurred at an annealing temperature of 350 °C. As the annealing temperature increases from 250 °C to 350 °C, the defect concentration was reduced, and the nanomembranes align themselves while forming a highly conductive printed graphene film, which is consistent with the TEM measurements on our samples as well.

It is not surprising that operating ink-jet printed graphene films at high power levels may have the potential for increased Joule heating, which can change the crystalline and electronic properties of the printed graphene films at these high-thermal/power conditions. We proceeded further with the Raman measurements of the printed multilayer graphene films to conduct temperature-dependent Raman measurements from 24.4 °C to 600 °C, where the data is shown in figure 4(c). When defects are present, it gives rise to two other features in the Raman spectra at ~1350 cm^{-1} (D band) and 1615 cm^{-1} (D′ band). The D′ band appears as a small shoulder on the G band, and the intensity of the D′ band is relatively small compared to the D band [30]. Clear peak shift in the G band is seen toward lower wave numbers with increasing temperature, similar to the case for the D′ band which gets more pronounced in intensity at 600 °C compared to room temperature. Previous investigations have demonstrated that electron-phonon coupling plays an important role in the temperature dependence of the G band shift [31]. The thermal expansion coefficient (TEC) is an important thermal and mechanical performance parameter of the printed multilayer graphene films, which can be estimated from the Raman data. The TEC of the printed graphene film was estimated from the G and G′ band Raman peak position shift and the data are shown in figures 4(e) and (f), respectively. Near room temperature (24.4 °C) printed multilayer graphene films exhibit a G band near

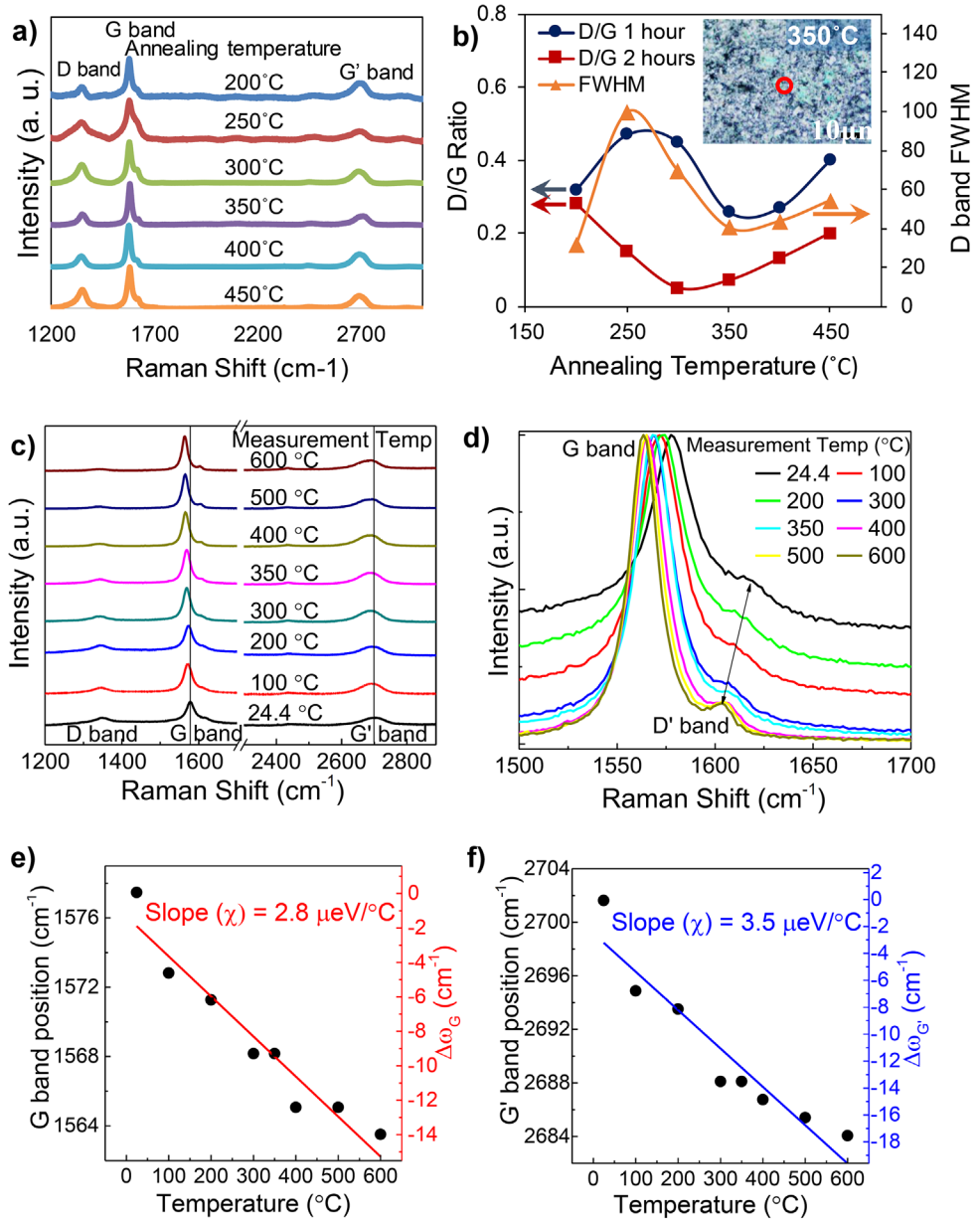

Figure 4. Raman analysis of the printed multilayer graphene films. (a) Raman shift as a function of annealing temperature for ink-jet printed graphene. (b) Change in the D/G ratio for samples annealed at 1 and 2 h; secondary axis indicating FWHM of the D band corresponding to 1 h annealing time. (c) Raman shift as a function of temperature for the sample annealed at 350 °C, 1 h. (d) Change in position of G and D′ band as measured at different temperatures for the 1 h 350 °C annealed sample. (e) Linear fit showing the extracted $\chi_G \sim 2.8\ \mu eV\ °C^{-1}$ for the G-band and (f) $\chi_{G'} \sim 3.5\ \mu eV\ °C^{-1}$ for the G′ band.

1577.4 cm^{-1}; however, it decreased to 1563.5 cm^{-1} with increased temperature up to 600 °C, which resulted in a G band peak shift in printed graphene films close to 14 cm^{-1}, as shown in figure 4(e). Similarly, the peak shift in the G′ band was observed to be nearly 17.5 cm^{-1} as shown in figure 4(f) (from 2701 cm^{-1} at 24.4 °C to 2684 cm^{-1} at 600 °C). These results in printed multilayer graphene films match previously investigated single and few layered graphene films on different substrates [26]. Higher shift with increasing temperature in the G′ band (17.5 cm^{-1}), compared to G band (14 cm^{-1}) matches previously investigated CVD grown graphene films on copper substrates, highlighting the double resonance processes in the G′ band, which were more sensitive to the changes in the electronic band structure than due to temperature induced strain [32]. On the contrary, the G mode is an optical phonon with zero vector which is very sensitive to carrier density instead of strain [28, 29]. The temperature dependence of the G and G' mode frequency shift in printed multilayer graphene films can be represented by the following relation: $\omega = \omega_0 + \chi T$, where ω_0 is the Raman frequency shift when the temperature T is extrapolated to 0 K, and χ is the first-order temperature coefficient determined by the slope of the linear fit. The extracted negative value of the G band temperature coefficient χ_G was ~2.8 $\mu eV\ °C^{-1}$, which is smaller compared to the G′ band temperature coefficient $\chi_{G'}$ (3.5 $\mu eV\ °C^{-1}$). Previous investigations have also shown χ_G to be smaller than $\chi_{G'}$ (~12 and 22 $\mu eV\ °C^{-1}$, respectively

[29]); however, we have found the values obtained in this work for χ_G and $\chi_{G'}$ are even smaller, indicating that our ink-jet printed graphene films should be less susceptible to thermal cycling.

The previous analysis of our ink-jet printed graphene films provided insights into the micro- and nanostructure of our material, which guided the design of a resistive, high-power structure that was constructed on both rigid and flexible and transparent substrates, and exhibited high-performance characteristics which we now describe in more detail here. High-power resistive structures have applications as temperature sensors, heating elements, current limiters, or in thermal management as heat spreaders to facilitate heat transfer [20, 33]. In this work, the power handling and dissipation characteristics of our ink-jet printed device was evaluated, and cryogenic measurements of the electronic transport were conducted from 6 K to 350 K from which the TCR, and other parameters were tabulated. The operational power of the printed devices was investigated with different annealing temperatures to examine their high power operational capabilities. Figure 5(a) shows output power variations of samples that were annealed for 1 h (top graph) and 2 h (bottom graph), where the data shows the power response for samples annealed from 300 °C to 450 °C. The highest output power of the printed graphene films was obtained for samples annealed at 350 °C for both the 1 h and 2 h cases. However, analysis of the annealing time shows that the sample annealed at the 1 h time exhibited an ability to deliver 90 μW of power at 1 V, which was higher compared to the sample annealed for 2 h that delivered 20 μW at 1 V. Our ink-jet printed multilayer graphene devices exhibited very low R (43 kΩ) and consequently very high output current and power compared to previous investigations (up to 600 MΩ and 4 MΩ in [21, 34], respectively). Due to this reason, we expected very high power operation in our printed devices. Figure 5(b) shows the temporal output power variations when increasingly higher applied voltages were applied. The power increased up to 7 W when the applied voltage increased to 90 V, at which point Joule heating at the contacts limited the transport. This measurement clearly shows the potential of our ink-jet printed multilayer graphene devices to operate under extremely high output power conditions, approaching ~10 W. According to our knowledge this was significantly higher compared to previous investigations (5 mW in [34]), and strongly highlights the opportunity to apply our ink-jet printed multilayer graphene films for high power applications for flexible electronics.

In order to better understand the electronic transport characteristics of our ink-jet printed multilayer graphene resistors, we conducted R–T measurements of our devices from 6 to 350 K from which the TCR and thermal index were computed. To conduct this measurement, first a mask was prepared on a transparency, as shown in the top, left inset of figure 5(c), in order to lithographically define regions where large Mo contacts were sputter deposited and patterned via lift-off. The multilayer graphene lines were then ink-jet printed to connect the Mo-contacts on which the probes for the cryogenic test were placed to ensure a good electrical contact without mechanically disrupting the network of nanomembranes from the ink-jet printed graphene for this thermal transport test. The fabricated device is shown at the bottom left inset of figure 5(c), while the magnified image in the bottom right inset of figure 5(c) clearly shows the ink jet printed line bridging the Mo electrodes. Figure 5(d) shows the R versus T Characteristic of the structures, and the inset demonstrates ln R with 1000/T for two different annealing conditions (250 °C and 350 °C annealed for 1 h). It is obvious that the sample annealed at 250 °C showed consistently higher R values (e.g. 82.79 kΩ at 140 K) when compared to the sample annealed at the higher temperature (e.g. 2.92 kΩ at 140 K). This data was fit to the Arrhenius model, denoted by equation (1) below:

$$R(T) = R_o \exp\left(\frac{E_a}{2kT}\right) = R_o \exp\left(\frac{B}{T}\right) \qquad (1)$$

where $R(T)$ is the R at temperature T, R_o is the R at $T = \infty$, E_a is the thermal activation energy as noted previously, k is the Boltzmann constant, and B is the thermal index. equation (1) can be rewritten as:

$$\ln R = \ln R_o + \frac{E_a}{2kT} = \ln R_o + \frac{B}{T} \qquad (2)$$

where a linear relationship is expected between the ln$R(T)$ versus T plot. When plotting ln$R(T)$ as a function of 1000/T (inset of figure 5(d)), the thermal parameters B, E_a and TCR were extracted, and were tabulated to be 14 K, 2.4 meV and 0.015%, respectively. These values are also shown in table 1 which compares our results to other material systems noted from prior work.

Both annealing conditions resulted in very small thermal index ($B \sim 14$ K) over the T range studied and a negative TCR behavior was evident in both cases. In general, most materials display much larger TCR values, but a few limited materials show NZ-TCR behavior [35], including graphene based hybrid systems where reduced-graphene oxide was used to decorate CVD-grown graphene [36]. High TCR materials demonstrated earlier (such as graphene) [20, 34] exhibited TCR values of ~1.14 % with B and $E_a \sim 1034$ K and 177 meV, respectively (see table 1). These types of materials are primarily used for thermistors, temperature sensing devices, and heating applications [37]. The printed graphene film demonstrated here falls in the low TCR category, and materials with low TCR or NZ-TCR can be used in a wide range of applications such as resistors in high precision electric heating systems, thermoelectric devices, micro heaters and other areas where a constant R over a range of temperatures is desired [35]. Our analysis shows that our devices exhibited the lowest reported TCR values amongst 2DLMs, though the work of Sun *et al* [36] shows TCR values that were also determined to be low for hybrid chemi-

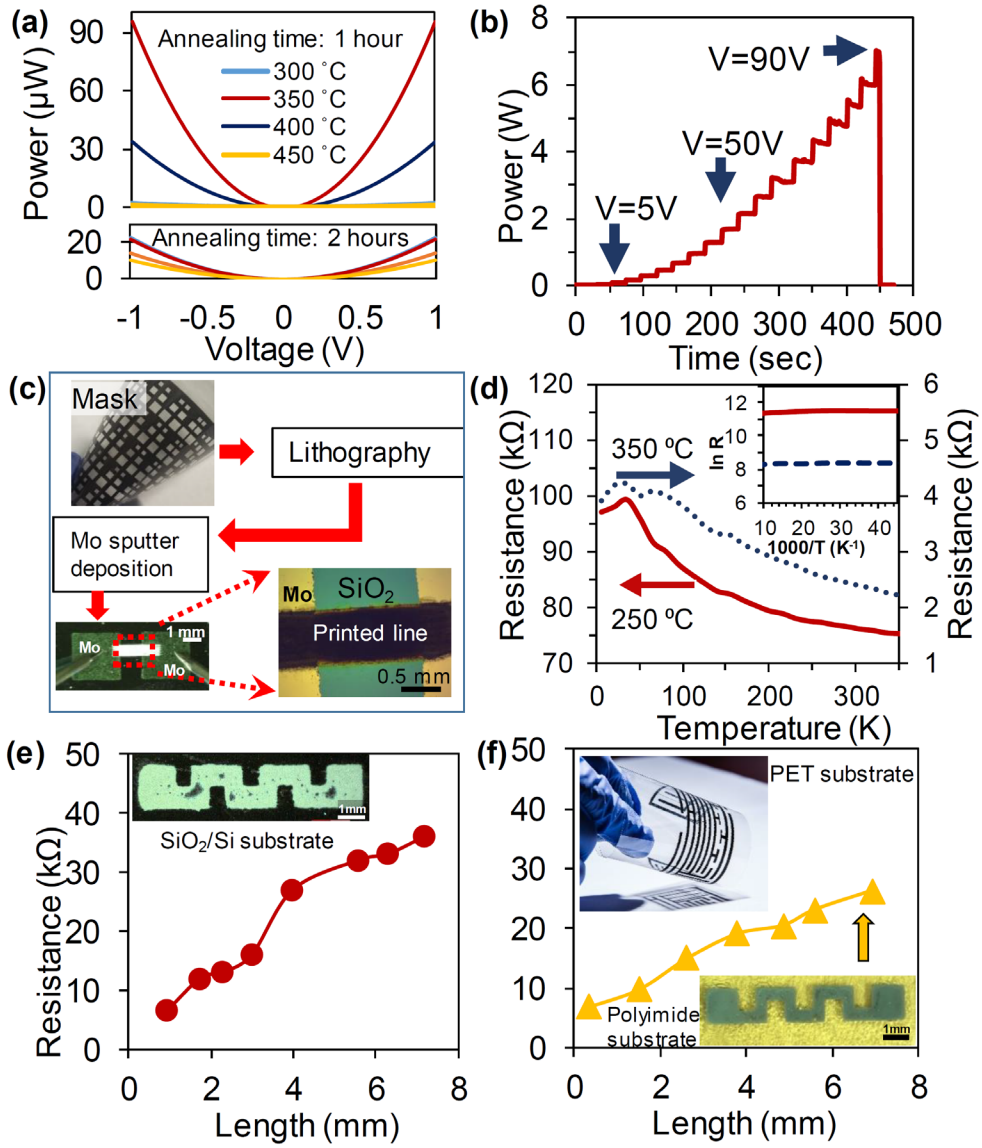

Figure 5. (a) Output power variation for the printed devices after 1 (top) and 2 h (bottom) of annealing time. (b) Temporal output power variation as increased voltages were applied to the device which shows the ability of the structure to deliver 7 W of power. (c) Process flow used to prepare the samples for *R*–*T* measurements depicted in (d), where the variation of *R* with *T* is illustrated for samples annealed at 250 °C and 350 °C; logarithmic plot shown in inset of ln(*R*) as a function of 1000/*T*. (e) *I*–*V* comparison of printed ink on both (e) SiO_2/Si, and on (f) polyimide substrates for 1 h of annealing time; top inset showing optical image of a printed pattern on PET substrate and bottom inset is an image of a resistive structure printed on polyimide substrate.

cal vapor deposited graphene-reduced graphene oxide systems, where the analysis was conducted in the heated regime from 303 K–573 K. Simultaneously, the printed multilayer graphene film demonstrated the ability to deliver very high power levels ~7 W without degrading or failing (see figure 5(b)). Therefore, the printed graphene film demonstrated in this work will be extremely valuable for high-power flexible electronics applications, with the unique low TCR feature at the same time.

The previous results allow us to propose a model to explain the *R* response of the prepared material with temperature. The total *R* of the composite film is the result of the addition of the temperature dependent contributions of the *R* from various sources which are indicated below in equation (3).

$$\rho_{\text{composite}}(T) = \sum \rho_{\text{G}}(T) + \rho_{\text{interface}}(T) + \rho_{\text{defects}}(T) + \rho_{\text{EC}}(T) \quad (3)$$

Here $\rho_{\text{composite}}$ represents the *R* of our overall ink-jet printed composite structure, ρ_{G} is the intrinsic *R* of the multilayer graphene membranes, $\rho_{\text{interface}}$ is the *R* at the interfacial junctions between nanomembranes, ρ_{defects} is the *R* due to defects within the nanomembranes and ρ_{EC} is the R due to the remnant EC/solvent; (T) indicates that these terms all have their unique *T* dependencies, and the overall resistivity or $\rho_{\text{composite}}$ is a sum over all of these ensemble contributions. Our previous discussion on the Raman data demonstrated the presence of the prominent G peak which indicates that the multilayer

Table 1. Comparison between high, low and NZ-TCR materials indicating thermal index B, activation energy E_a, and TCR values from prior reports.

Temperature response	Material	Thermal index B (K)	Activation Energy E_a (meV)	TCR (%K^{-1})	Reference
High TCR	Graphene	1034	177.84	−1.148	[34]
	Graphene	946	167.2	−1.05	[20]
Low TCR	Printed multilayer graphene film	14	2.4	−0.015	This work
NZ-TCR	Carbon nanotube + carbon black	5	0.86	−0.005	[22]
	Antiperovskite $Mn_3Ni_{1-x}Cu_xN$	2	0.34	−0.002	[35]

graphene is dominant in the composite, and so the contribution from other components such as remnant EC should be minimal in the thermal response, though a more thorough investigation is necessary to rule out the contribution from the remnant EC. The contribution from the $\rho_{interface}$ should also be minimal since at higher temperatures there should be more energy for electrons to tunnel across the interface reducing R, which we do not observe strongly here. We believe the contribution from the defects is dominating the temperature dependence of the electronic transport, where the D/G ratio was seen to be ~0.26 from Raman spectroscopy in the ink jet printed films, while the TEM also showed dark agglomerations for samples annealed at 350 °C (e.g. figure 3(e)). The slight negative TCR dependence with $E_a \sim 2.4$ meV represents a small energy activation barrier for electron hopping that explains the negative TCR, but the generally temperature insensitive R is suggestive of transport limited by defects, which we have exploited judiciously to our advantage to demonstrate a practical device for flexible electronics.

The prepared ink was also printed on flexible polyimide and polyethylene terephthalate (PET) substrates. Figures 5(e) and (f) show R values for multilayer graphene inks printed on rigid SiO_2/Si substrates and on flexible polyimide substrates, respectively, with the insets in both figures reflecting printed structures on the various rigid, flexible and transparent PET substrates. The R scaled linearly as the probe separation distance increased in both figures 5(e) and (f), as expected. However, for the case of the polyimide substrate (figure 5(f)), the R was generally lower, which may be due to better adherent properties of the multilayer graphene ink on the carbon based polyimide substrate compared to SiO_2/Si.

Conclusions

A high-power and low-TCR device was successfully ink-jet printed using graphene dispersions. The printing conditions for the device were optimized, which showed the ideal number of active nozzles was 2–4, and that 30 printing passes resulted in a uniform, low-resistance channel region. Characterization conducted using SEM, TEM and Raman spectroscopy analysis showed that the optimum annealing temperature and time were 350 °C and 1 h, respectively. A practical device was ink-jet printed at these conditions which successfully showed that a high-power resistive structure was operational up to 7 W, without failing and at the same time it yielded a thermally—invariant resistance response with low TCR values, which is believed to be lowest reported amongst 2DLMs. Due to the resistive heating capability of the structures designed here, our device has the potential to be useful for high-power flexible electronics applications.

Methods

Materials: The ink used in this work was prepared by sonicating commercially available graphite rod pieces (Sigma Aldrich #496553) at a concentration of 6 mg ml^{-1} in N-methyl-2-pyrrolidone (NMP) for 24 h. After the sonication, 4%wt Ethyl Cellulose (EC) (Sigma Aldrich 200646) was added to the dispersion and sonicated for another 4 h. The ink was separated after allowing the dispersion to stabilize overnight and selecting only the supernatant to avoid any precipitates that may contain bigger particles. *Printing*: The DIMATIX 2831 material printer from Fujifilm was used for the ink-jet printing, where the ink cartridges were purchased from the manufacturer and had a volume of 10 pl. The cartridges comprised of 16 nozzles with a nozzle diameter of ~21.5 μm. *Characterization:* SEM microscopy was carried out in a Hitachi S-4800. The TEM analysis was conducted using a TEM 2100F field emission gun. The Raman data was obtained using a Horiba LabRAM HR Evolution where the excitation laser wavelength used was 532 nm. Electrical characterization was conducted using a micromanipulator 450PM-B probe stage equipped with a HP precision semiconductor parameter analyzer 4156A. A Lakeshore CRX–4 K probe station was used to obtain the R versus T data with a Keysight B1500-A Semiconductor Device Analyzer. Profilometer measurements were performed on the Brocker Dektak XT Stylus Profiler. *Substrate:* SiO_2/Si wafers with a 300 nm oxide layer and polyimide substrates were used for drop casting and printing.

Acknowledgments

ABK acknowledges the University of Texas System Faculty Science and Technology Acquisition and Retention (STARS) award (EC284802) for the acquisition of equipment in the establishment of

the Nanomaterials and Devices Lab at the University of Texas, El Paso (UTEP). Support provided by the UTEP start up grant is also acknowledged for MM. We also thank the Army Research Office (ARO W911NF-15-1-0425) that enabled us to pursue this work. Additionally, we thank Dr Deidra Hodges for the Mo-deposition.

Notes

The authors declare no competing financial interest.

References

[1] International Technology Roadmap for Semiconductors (ITRS) 2.0 2015 *Executive Report* www.itrs2.net/itrs-reports.html
[2] Courtland R 2016 Transistors could stop shrinking in 2021 *IEEE Spectr.* **53** 9–11
[3] Secor E B and Hersam M C 2015 Emerging carbon and post-carbon nanomaterial inks for printed electronics *J. Phys. Chem. Lett.* **6** 620–6
[4] Cai L and Wang C 2015 Carbon nanotube flexible and stretchable electronics *Nanoscale Res. Lett.* **10** 1–21
[5] Cook B, Tehrani B, Cooper J, Kim S and Tentzeris M 2015 Integrated printing for 2D/3D flexible organic electronic devices *Handbook of Flexible Organic Electronics* (Cambridge : Woodhead) pp 199–216
[6] Muccini M A 2006 Bright future for organic field-effect transistors *Nat. Mater.* **5** 605–13
[7] Huang L, Huang Y, Liang J, Wan X and Chen Y 2011 Graphene-based conducting inks for direct inkjet printing of flexible conductive patterns and their applications in electric circuits and chemical sensors *Nano Res.* **4** 675–84
[8] Coleman J, Lotya M, O'Neill A, Bergin S, King P, Khan U, Young K, Gaucher A, De S and Smith R 2011 Two-dimensional nanosheets produced by liquid exfoliation of layered materials *Science* **331** 568–71
[9] Li J, Lemme M C and Östling M 2014 Inkjet printing of 2D layered materials *ChemPhysChem* **15** 3427–34
[10] Joong T H, Jeong I J, Haena K, Jun Y H, Hyung K Y and Jong S W 2014 Extremely efficient liquid exfoliation and dispersion of layered materials by unusual acoustic cavitation *Sci. Rep.* **4** 5133
[11] Viculis L, Mack J and Kaner R A 2003 Chemical route to carbon nanoscrolls *Science* **299** 1361
[12] Gao Y, Shi W, Wang W, Leng Y and Zhao Y 2014 Inkjet printing patterns of highly conductive pristine graphene on flexible substrates *Ind. Eng. Chem. Res.* **53** 16777–84
[13] Chen G, Weng W, Wu D, Wu C, Lu J, Wang P and Chen X 2004 Preparation and characterization of graphite nanosheets from ultrasonic powdering technique *Carbon* **42** 753–9
[14] Jana M, Saha S, Khanra P, Samanta P, Koo H, Murmu N C and Kuila T 2015 Non-covalent functionalization of reduced graphene oxide using sulfanilic acid azocromotrop and its application as supercapacitor electrode material *J. Mater. Chem.* A **3** 7323–31
[15] Dreyer D R, Park S, Bielawski C W and Ruoff R S 2010 The chemistry of graphene oxide *Chem. Soc. Rev.* **39** 228–40
[16] Giardi R, Porro S, Chiolerio A, Celasco E and Sangermano M 2013 Inkjet printed acrylic formulations based on UV-reduced graphene oxide nanocomposites *J. Mater. Sci.* **48** 1249–55
[17] Behabtu N, Lomeda J R, Green M J and Higginbotham A L 2010 Spontaneous high-concentration dispersions and liquid crystals of graphene *Nat. Nanotechnol.* **5** 406–11
[18] Di W, Hongwei L, Dongxue H and Qixian Z 2011 Properties of graphene inks stabilized by different functional groups *Nanotechnology* **22** 245702
[19] Lotya M, Hernandez Y, King P J, Smith R J and Nicolosi V 2009 Liquid phase production of graphene by exfoliation of graphite in surfactant/water solutions *J. Am. Chem. Soc.* **131** 3611–20
[20] Yan C, Wang J and Lee P S 2015 Stretchable graphene thermistor with tunable thermal index *ACS Nano* **9** 2130–7
[21] Kong D, Le L T, Li Y, Zunino J L and Lee W 2012 Temperature-dependent electrical properties of graphene inkjet-printed on flexible materials *Langmuir* **28** 13467–72
[22] Chu H, Lee S C, Lee S, Kim D, Moon C and Park S H 2015 Smart conducting polymer composites having zero temperature coefficient of resistance *Nanoscale* **7** 471–8
[23] Shah R and Hughey S L 1986 Method of making zero temperature coefficient of resistance resistors *US Patent* 4,579,600
[24] Michel M, Desai J A, Biswas C and Kaul A B 2016 Engineering chemically exfoliated dispersions of two-dimensional graphite and molybdenum disulphide for ink-jet printing *Nanotechnology* **27** 485602
[25] Michel M, Desai J A, Biswas C and Kaul A B 2016 Optimization of fluid characteristics of 2D materials for inkjet printing *MRS Adv.* **1** 2199–206
[26] Calizo I, Balandin A, Bao W, Miao F and Lau C 2007 Temperature dependence of the Raman spectra of graphene and graphene multilayers *Nano Lett.* **7** 2645–9
[27] Vidano R, Fischbach D, Willis L and Loehr T 1981 Observation of Raman band shifting with excitation wavelength for carbons and graphites *Solid State Commun.* **39** 341–4
[28] Ferrari A C 2007 Raman spectroscopy of graphene and graphite: disorder, electron–phonon coupling, doping and nonadiabatic effects *Solid State Commun.* **143** 47–57
[29] Wang W, Peng Q, Dai Y, Qian Z and Liu S 2016 Temperature dependence of raman spectra of graphene on copper foil substrate *J. Mater. Sci.* **27** 3888–93
[30] Eckmann A, Felten A, Mishchenko A, Britnell L, Krupke R, Novoselov K S and Casiraghi C 2012 Probing the nature of defects in graphene by raman spectroscopy *Nano Lett.* **12** 3925–30
[31] Tian S, Yang Y, Liu Z, Wang C, Pan R, Gu C and Li J 2016 Temperature-dependent Raman investigation on suspended graphene: contribution from thermal expansion coefficient mismatch between graphene and substrate *Carbon* **104** 27–32
[32] Allen M J, Fowler J D, Tung V C, Yang Y, Weiller B H and Kaner R B 2008 Temperature dependent Raman spectroscopy of chemically derived graphene *Appl. Phys. Lett.* **93** 193119
[33] Renteria J D, Nika D L and Balandin A A 2014 Graphene thermal properties: applications in thermal management and energy storage *Appl. Sci.* **4** 525–47
[34] Al-Mumen H, Rao F, Dong L and Li W 2013 Design, fabrication, and characterization of graphene thermistor *8th IEEE Int. Conf. on Nano/Micro Engineered and Molecular Systems (NEMS)* pp 1135–8
[35] Ding L, Wang C, Chu L, Yan J, Na Y, Huang Q and Chen X 2011 Near zero temperature coefficient of resistivity in antiperovskite $Mn_3Ni_{1-x}Cu_xN$ *App. Phys. Lett.* **99** 251905
[36] Sun P, Zhu M, Wang K, Zhong M, Wei J, Wu D and Zhu H 2013 Small temperature coefficient of resistivity of graphene/graphene oxide hybrid membranes *ACS Appl. Mater. Interfaces* **5** 9563–71
[37] Kang J, Kim H, Kim H S, Lee S K, Bae S, Ahn J H and Hong B H 2011 High-performance graphene-based transparent flexible heaters *Nano Lett.* **11** 5154–58